INTERNATIONAL JOURNAL FOR NUMERICAL AND ANALYTICAL METHODS IN GEOMECHANICS
Int. J. Numer. Anal. Meth. Geomech. 2014; **38**:1078–1100
Published online 21 December 2013 in Wiley Online Library (wileyonlinelibrary.com). DOI: 10.1002/nag.2249

Development of the distinct lattice spring model for large deformation analyses

G.-F. Zhao*,†

Centre for Infrastructure Engineering and Safety, School of Civil and Environmental Engineering, The University of New South Wales, Sydney, NSW 2052, Australia

SUMMARY

This study develops the distinct lattice spring model (DLSM) for geometrically nonlinear large deformation problems. The formulation of a spring bond deformation under a large deformation is derived under the Lagrange framework using polar decomposition. The results reveal that the DLSM's stiffness matrix under small deformations is the tangent stiffness matrix of the DLSM under large deformations. The formulation of the spring bond internal force under a given configuration is also presented and can be used to calculate the unbalanced force. Using these formulations, three nonlinear solving methods (the Euler method, modified Euler method, and Newton method) are developed for the DLSM with which to tackle large deformation problems. To investigate the performance of the developed model, three numerical examples involving large deformations are presented, the results of which are also in good agreement with the analytical and finite element method solutions. Copyright © 2013 John Wiley & Sons, Ltd.

Received 30 May 2013; Revised 7 September 2013; Accepted 11 November 2013

KEY WORDS: lattice spring model; large deformation; nonlinear; polar decomposition

1. INTRODUCTION

Large deformations and geometrically nonlinearity are crucial components of many engineering problems. Many numerical methods have been developed to tackle the problem of solving them, such as the finite element method (FEM) [1–8], the boundary element method (BEM) [9–11], the meshless method [12–14], the Lagrangian integration point FEM [15], the natural element method (NEM) [16], the local Kriging method [17], the nearest-nodes FEM [18], and the B spline-based method [19]. Various approaches have been developed to implement a numerical method for large deformation analyses, including the total Lagrangian (TL) approach [1,2,19], the updated Lagrangian (UL) approach [3,4,14,18], the arbitrary Lagrangian–Eulerian (ALE) technique [5,20], the corotational approach [8], and the remeshing and interpolation technique with small strain model (RITSS) method [6]. Each method has its own advantages—for example, the meshless method is free of meshing requirements (e.g. [12–14]), whereas the RITSS FEM by Hu and Randolph [6] is robust and easy to implement. It has also been found that different approaches and methods can produce very similar results (e.g. [14,17,19]), and large-deformation FEM has usually been adopted as the reference method for benchmarking. The development of a specific numerical method for large deformation analysis is an essential extension of this method to the area of nonlinear analysis, which can usually be classified as geometric nonlinearity and material nonlinearity. Large deformation problems may involve both geometric and material nonlinearity, but this work considers only geometric nonlinearity.

*Correspondence to: G-F. Zhao, Centre for Infrastructure Engineering and Safety, School of Civil and Environmental Engineering, The University of New South Wales, Sydney, NSW 2052, Australia.
†E-mail: gaofeng.zhao@unsw.edu.au

The lattice spring model (LSM) was originally developed by Hrennikoff [21] to solve continuum elasticity problems with Poisson's ratio fixed at 1/3. The model was underdeveloped due to computational limitations and the subsequent development of the FEM. Furthermore, the LSM's Poisson's limitation has also handicapped its further application because classical LSM can solve problems only at a fixed Poisson's value, such as 1/3 in two-dimensional plane-stress cases and 1/4 in three-dimensional cases. However, due to the LSM's suitability for fracturing simulations of solids, many researchers have renewed their interest in this method in recent years. A review of recent LSM development can be found in [22,23]. The concept of LSM has widely been used for large deformation problems in computational graphics, such as for hair dynamics simulation [24] and cloth simulation [25]. These models are called mass-spring models and focus more on realistic visual effects than realistic mechanical responses. For example, Selle et al. [24] have used a tetrahedron element with additional hidden springs to represent a single spring bond and produce realistic bounce-back behaviour in soft material. However, the model considers only the central interactions between particles, which means the Poisson's limitation is less important to the computational graphics but very crucial to the mechanical analysis. Work has also been done on the mechanical application of the LSM to large deformation problems. For example, Holecek and Moravec [26] have built a 'ball-and-spring' model to represent certain features of hyperelastic materials, Hou [27] has developed a lattice model to simulate the fracture behaviour of large strain composites, and Patete et al. [28] have presented a mass-spring model for large deformation analyses in biomechanics during computer-assisted breast surgeries. Nevertheless, these models have still considered only the normal spring and central interactions between particles, and maintain the Poisson's limitation of Hrennikoff's model.

This study further develops the distinct lattice spring model (DLSM) [29, 30] for large deformation analyses. In DLSM, the restriction on the Poisson's ratio in classical LSM has been solved through a technique to evaluate spring deformation using the local strain technique rather than the particle displacements directly. The ability of DLSM to model elastic problems with different Poisson's ratios has been verified by many numerical examples. Nevertheless, these examples all involve small deformations and do not account for the influence of geometric nonlinearity. In this work, the DLSM is further developed to solve large deformation problems. First, the formulation of a spring bond deformation under a large deformation is derived using polar decomposition. Next, the tangent stiffness matrix of the DLSM under a large deformation is proven equal to the stiffness matrix of the DLSM under a small deformation. Formulations to calculate the internal spring bond force and unbalanced force are also derived and used to develop three nonlinear solving methods. Finally, the model is validated by solving three large deformation problems.

2. MODEL

The DLSM was presented as an explicit three-dimensional model for dynamic analysis [29]. The implicit two-dimensional DLSM was developed for static problems later [30], which is further developed in this work. The basic principle of DLSM is to represent a material by particles linked through spring bonds (see Figure 1). In two-dimensional cases, there are two types of spring bond, a three-particle spring bond (Type-I in Figure 1) and a four-particle spring bond (Type-II in Figure 1). The bond is made up from one normal spring and one shear spring as illustrated in Figure 1a. The lattice structure can either use the edge model of a FEM mesh (e.g. [23,30]) or the lattice structure from a particle model (e.g. [31]). The internal force and strain energy are both stored in the spring bonds and the spring bond deformation is evaluated from the local strain of the particle cluster. The spring bond's displacement function can be obtained by using the shape function of a linear triangular FEM element or from the moving least square (MLS) over the four particles [30]. In DLSM, the spring bond deformation under the local coordinate can be written as:

$$\widehat{\mathbf{u}} = \begin{pmatrix} u^n \\ u^s \end{pmatrix} = \mathbf{C}\mathbf{u} \tag{1}$$

DOI: 10.1002/nag

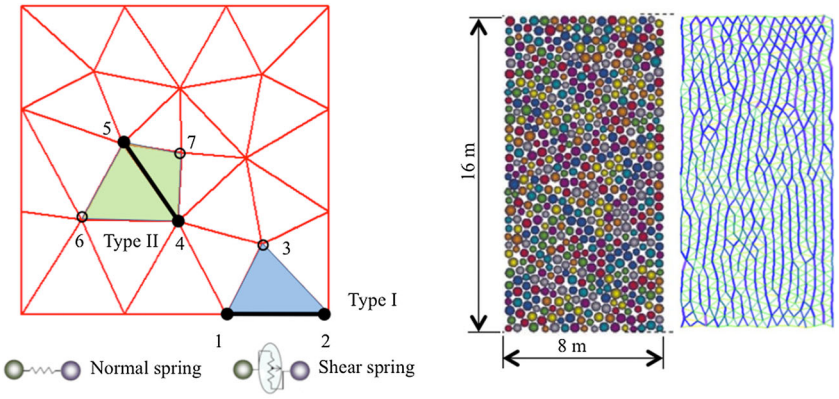

Figure 1. Two-dimensional lattice spring model and two bond types: (a) Lattice model based on FEM mesh and (b) Lattice model from a particle model [31].

where **C** is an interpolation matrix that is constant for a given spring bond element (see Figure 1) due to its being determined by the initial position of the particles in the cluster, $\widehat{\mathbf{u}}$ is the local bond deformation, u^n is the bond's normal deformation, u^s is the bond's shear deformation, and **u** is the displacement vector of the particles in the cluster. The details of this expression and the derivation of Equation (1) can be found in [30]. Equation (1) has been derived under a small deformation assumption and does not consider geometric nonlinearity. The following section presents a more general formulation with which to consider large deformation.

2.1. *Formulation of spring bond deformation under a large deformation*

As shown in Figure 2a, assume a spring bond is embedded in a cube. According to polar decomposition, a general deformation can be decomposed into a rigid rotation ω and an objective Cauchy strain term $\left(\hat{\varepsilon}_x, \hat{\varepsilon}_y, \hat{\varepsilon}_{xy}\right)^{\mathrm{T}}$ [32]. The objective Cauchy strain indicates that the strain is rigidly rotationally invariant; that is, the Cauchy strain is evaluated after removing all the rigid rotation of a deformation. Here, a general deformation is applied to the cube in a sequential manner. First, a rigid rotation ω is applied to the cube (see Figure 2b). For a given point $(x^0,y^0)^{\mathrm{T}}$ in the cube, its new position becomes:

$$\begin{pmatrix} x^1 \\ y^1 \end{pmatrix} = \begin{pmatrix} \cos\omega & -\sin\omega \\ \sin\omega & \cos\omega \end{pmatrix} \begin{pmatrix} x^0 \\ y^0 \end{pmatrix} \tag{2}$$

Next, a rigid translation $(u_0,v_0)^{\mathrm{T}}$ is applied to the cube and the new position of the point $(x^0,y^0)^{\mathrm{T}}$ can be given as:

$$\begin{pmatrix} x^2 \\ y^2 \end{pmatrix} = \begin{pmatrix} x^1 \\ y^1 \end{pmatrix} + \begin{pmatrix} u_0 \\ v_0 \end{pmatrix} \tag{3}$$

Under the rotated configuration $\hat{x} - \hat{o} - \hat{y}$ (see Figure 2c), a Cauchy strain deformation $\left(\hat{\varepsilon}_x, \hat{\varepsilon}_y, \hat{\varepsilon}_{xy}\right)$ is applied to the cube that causes the point to have the displacement:

$$\begin{pmatrix} \hat{u} \\ \hat{v} \end{pmatrix} = \begin{pmatrix} \hat{x}^0 & 0 \\ 0 & \hat{y}^0 \end{pmatrix} \begin{pmatrix} \hat{\varepsilon}_x \\ \hat{\varepsilon}_y \end{pmatrix} + \begin{pmatrix} \hat{y}^0 \\ \hat{x}^0 \end{pmatrix} \hat{\varepsilon}_{xy} \tag{4}$$

The corresponding displacement at the original coordinate (see Figure 2a) can be expressed as:

DOI: 10.1002/nag

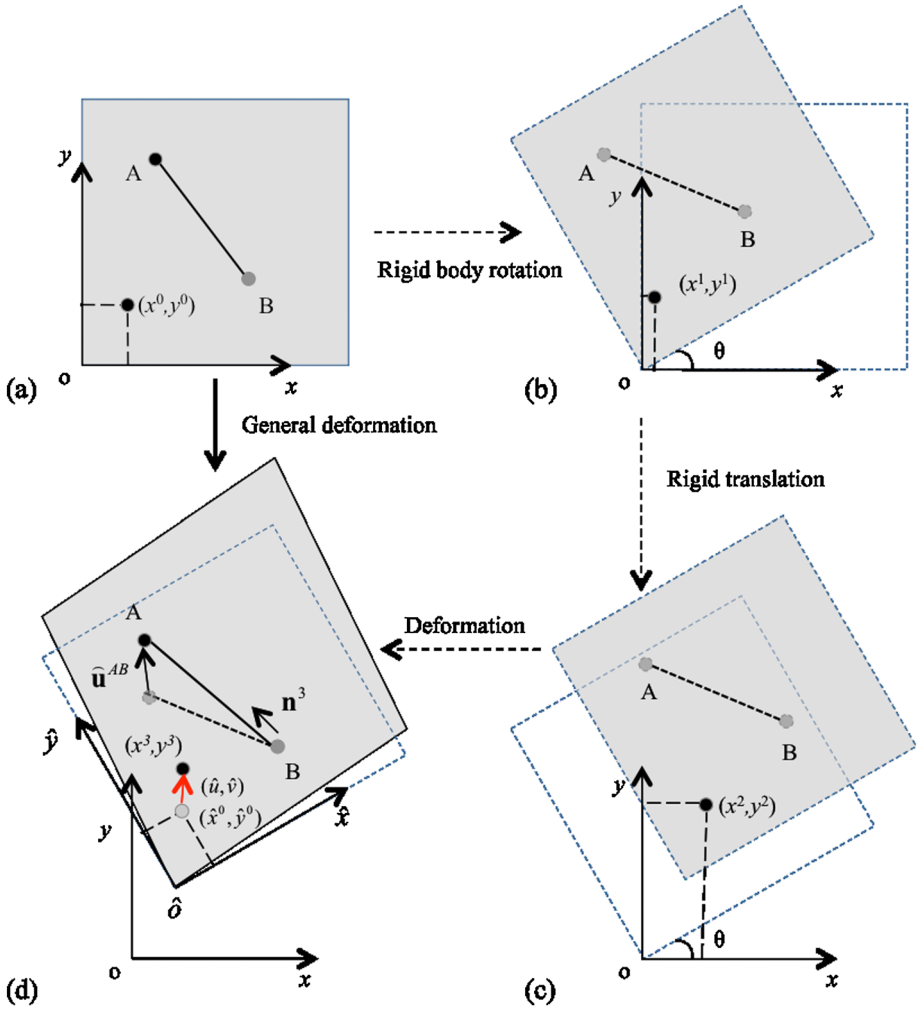

Figure 2. Deformation of a cube unit with a bond connecting two particles: (a) initial state, (b) intermediate state after rigid rotation, (c) intermediate state after rigid translation, and (d) final state.

$$\begin{pmatrix} u \\ v \end{pmatrix} = \begin{pmatrix} \cos\omega & \sin\omega \\ -\sin\omega & \cos\omega \end{pmatrix} \begin{pmatrix} \hat{u} \\ \hat{v} \end{pmatrix} \tag{5}$$

Combining Equations (2), (3), and (5), the final position of the point $(x^0,y^0)^{\mathrm{T}}$ is:

$$\begin{pmatrix} x^3 \\ y^3 \end{pmatrix} = \begin{pmatrix} \cos\omega & -\sin\omega \\ \sin\omega & \cos\omega \end{pmatrix} \begin{pmatrix} x^0 \\ y^0 \end{pmatrix} + \begin{pmatrix} \cos\omega & \sin\omega \\ -\sin\omega & \cos\omega \end{pmatrix} \left(\begin{pmatrix} \hat{x}^0 & 0 \\ 0 & \hat{y}^0 \end{pmatrix} \begin{pmatrix} \hat{\varepsilon}_x \\ \hat{\varepsilon}_y \end{pmatrix} + \begin{pmatrix} \hat{y}^0 \\ \hat{x}^0 \end{pmatrix} \hat{\varepsilon}_{xy} \right) + \begin{pmatrix} u_0 \\ v_0 \end{pmatrix} \tag{6}$$

Because the rigid rotation cannot change the relative position of a point inside the cube, we have $(\hat{x}^0,\hat{y}^0)\equiv(x^0,y^0)$. Therefore, Equation (6) can be rewritten as:

$$\begin{pmatrix} x^3 \\ y^3 \end{pmatrix} = \begin{pmatrix} \cos\omega & -\sin\omega \\ \sin\omega & \cos\omega \end{pmatrix} \begin{pmatrix} x^0 \\ y^0 \end{pmatrix} + \begin{pmatrix} \cos\omega & \sin\omega \\ -\sin\omega & \cos\omega \end{pmatrix} \left(\begin{pmatrix} x^0 & 0 \\ 0 & y^0 \end{pmatrix} \begin{pmatrix} \hat{\varepsilon}_x \\ \hat{\varepsilon}_y \end{pmatrix} + \begin{pmatrix} y^0 \\ x^0 \end{pmatrix} \hat{\varepsilon}_{xy} \right) + \begin{pmatrix} u_0 \\ v_0 \end{pmatrix} \tag{7}$$

DOI: 10.1002/nag

Finally, the displacement of the point $(x^0,y^0)^{\mathrm{T}}$ under the original coordinate is:

$$\begin{aligned}\begin{pmatrix} u^3 \\ v^3 \end{pmatrix} &= \begin{pmatrix} \cos\omega & -\sin\omega \\ \sin\omega & \cos\omega \end{pmatrix}\begin{pmatrix} x^0 \\ y^0 \end{pmatrix} + \begin{pmatrix} \cos\omega & \sin\omega \\ -\sin\omega & \cos\omega \end{pmatrix}\left(\begin{pmatrix} x^0 & 0 \\ 0 & y^0 \end{pmatrix}\begin{pmatrix} \hat{\varepsilon}_x \\ \hat{\varepsilon}_y \end{pmatrix} + \begin{pmatrix} y^0 \\ x^0 \end{pmatrix}\hat{\varepsilon}_{xy}\right) + \begin{pmatrix} u_0 \\ v_0 \end{pmatrix} - \begin{pmatrix} x^0 \\ y^0 \end{pmatrix} \\ &= \begin{pmatrix} \cos\omega - 1 & -\sin\omega \\ \sin\omega & \cos\omega - 1 \end{pmatrix}\begin{pmatrix} x^0 \\ y^0 \end{pmatrix} + \begin{pmatrix} \cos\omega & \sin\omega \\ -\sin\omega & \cos\omega \end{pmatrix}\left(\begin{pmatrix} x^0 & 0 \\ 0 & y^0 \end{pmatrix}\begin{pmatrix} \hat{\varepsilon}_x \\ \hat{\varepsilon}_y \end{pmatrix} + \begin{pmatrix} y^0 \\ x^0 \end{pmatrix}\hat{\varepsilon}_{xy}\right) + \begin{pmatrix} u_0 \\ v_0 \end{pmatrix}\end{aligned} \tag{8}$$

Now, the relative displacement (or spring bond deformation) between two particles A and B in the cube can be calculated as:

$$\begin{aligned}\begin{pmatrix} u^{AB} \\ v^{AB} \end{pmatrix} = &\underbrace{\begin{pmatrix} \cos\omega - 1 & -\sin\omega \\ \sin\omega & \cos\omega - 1 \end{pmatrix}\begin{pmatrix} x^A - x^B \\ y^A - y^B \end{pmatrix}}_{\text{rigid rotation term}} + \\ &\underbrace{\begin{pmatrix} \cos\omega & \sin\omega \\ -\sin\omega & \cos\omega \end{pmatrix}\left(\begin{pmatrix} x^A - x^B & 0 \\ 0 & y^A - y^B \end{pmatrix}\begin{pmatrix} \hat{\varepsilon}_x \\ \hat{\varepsilon}_y \end{pmatrix} + \begin{pmatrix} y^A - y^B \\ x^A - x^B \end{pmatrix}\hat{\varepsilon}_{xy}\right)}_{\text{deformation term}}\end{aligned} \tag{9}$$

Due to the fact that the rigid rotation cannot cause strain energy in the cube, the spring bond deformation between two particles that can produce the internal force needed for strain energy is:

$$\widehat{\mathbf{u}} = \begin{pmatrix} \widehat{u}^{\,AB} \\ \widehat{v}^{\,AB} \end{pmatrix} = \begin{pmatrix} \cos\omega & \sin\omega \\ -\sin\omega & \cos\omega \end{pmatrix}\left(\begin{pmatrix} x^A - x^B & 0 \\ 0 & y^A - y^B \end{pmatrix}\begin{pmatrix} \hat{\varepsilon}_x \\ \hat{\varepsilon}_y \end{pmatrix} + \begin{pmatrix} y^A - y^B \\ x^A - x^B \end{pmatrix}\hat{\varepsilon}_{xy}\right) \tag{10}$$

Equation (10) is the formulation for a spring bond deformation under a general deformation. Because the spring bond can have a very large deformation, the normal direction of the spring may totally be different from the initial direction. Therefore, unlike in the small deformation case, large deformation analyses should use the normal direction of the deformed spring bond, which is written as:

$$\mathbf{n}^3 = \begin{pmatrix} \mathbf{n}_x^3 \\ \mathbf{n}_y^3 \end{pmatrix} = \begin{pmatrix} \dfrac{x_A^3 - x_B^3}{l^3} \\ \dfrac{y_A^3 - y_B^3}{l^3} \end{pmatrix} \tag{11}$$

The normal deformation of the spring bond can be calculated as:

$$u^n = \left(\mathbf{n}_x^3, \mathbf{n}_y^3\right)\begin{pmatrix} \widehat{u}^{\,AB} \\ \widehat{v}^{\,AB} \end{pmatrix} \tag{12}$$

While the shear deformation is:

$$u^s = \left(-\mathbf{n}_y^3, \mathbf{n}_x^3\right)\begin{pmatrix} \widehat{u}^{\,AB} \\ \widehat{v}^{\,AB} \end{pmatrix} \tag{13}$$

For a given deformation, the rigid rotation ω and the objective Cauchy strain $\left(\hat{\varepsilon}_x, \hat{\varepsilon}_y, \hat{\varepsilon}_{xy}\right)^{\mathrm{T}}$ can be obtained by polar decomposition. The deformation gradient matrix is:

DOI: 10.1002/nag

$$\mathbf{F} = \begin{pmatrix} 1+\dfrac{\partial u}{\partial x} & \dfrac{\partial u}{\partial y} \\ \dfrac{\partial v}{\partial x} & 1+\dfrac{\partial v}{\partial y} \end{pmatrix} = \begin{pmatrix} a & b \\ c & d \end{pmatrix} \tag{14}$$

The rigid rotation matrix of the right polar decomposition over $\mathbf{F}$ can be written as:

$$\mathbf{Q} = \begin{pmatrix} \cos\omega & \sin\omega \\ -\sin\omega & \cos\omega \end{pmatrix} = \begin{pmatrix} a & b \\ c & d \end{pmatrix} + sign(ad+bc)\begin{pmatrix} d & -c \\ -b & a \end{pmatrix} \tag{15}$$

The symmetric matrix $\mathbf{U}$ (deformation gradient matrix removed rigid rotation) can be obtained as:

$$\mathbf{U} = \mathbf{Q}^{\mathrm{T}}\mathbf{F} = \begin{pmatrix} e & f \\ f & h \end{pmatrix} \tag{16}$$

The objective Cauchy strain $\left(\hat{\varepsilon}_x, \hat{\varepsilon}_y, \hat{\varepsilon}_{xy}\right)^T$ can be calculated as:

$$\begin{pmatrix} \hat{\varepsilon}_x \\ \hat{\varepsilon}_y \\ \hat{\varepsilon}_{xy} \end{pmatrix} = \begin{pmatrix} e-1 \\ h-1 \\ f \end{pmatrix} \tag{17}$$

For a given deformation, the normal and shear spring deformation can now be calculated from Equations (10) to (17).

2.2. *Tangent stiffness matrix*

The spring bond deformation under a general deformation can be written in a form similar to that of Equation (1). According to Equations (10) to (13), the general deformation of the bond can be represented as

$$\begin{aligned} \widehat{\mathbf{u}} = \begin{pmatrix} u^n \\ u^s \end{pmatrix} &= \begin{pmatrix} \mathbf{n}_x^3 & \mathbf{n}_y^3 \\ -\mathbf{n}_y^3 & \mathbf{n}_x^3 \end{pmatrix} \begin{pmatrix} \cos\omega & \sin\omega \\ -\sin\omega & \cos\omega \end{pmatrix} \begin{pmatrix} x^A - x^B & 0 & y^A - y^B \\ 0 & y^A - y^B & x^A - x^B \end{pmatrix} \begin{pmatrix} \hat{\varepsilon}_x \\ \hat{\varepsilon}_y \\ \hat{\varepsilon}_{xy} \end{pmatrix} \\ &= \begin{pmatrix} \mathbf{n}_x^3 & \mathbf{n}_y^3 \\ -\mathbf{n}_y^3 & \mathbf{n}_x^3 \end{pmatrix} \begin{pmatrix} \cos\omega & \sin\omega \\ -\sin\omega & \cos\omega \end{pmatrix} \begin{pmatrix} x^A - x^B & 0 & y^A - y^B \\ 0 & y^A - y^B & x^A - x^B \end{pmatrix} \mathbf{C}_0(\mathbf{u})\mathbf{u} = \mathbf{C}(\mathbf{u})\mathbf{u} \end{aligned} \tag{18}$$

where $\mathbf{C}(\mathbf{u})$ is the interpolation matrix that accounts for geometric nonlinearity. The interpolation matrix cannot be determined by the initial position of the particle cluster, but rather requires the displacement of the particles.

Assume the material property does not change under the deformation (a pure geometric nonlinear problem) and the spring stiffness remains constant during the calculation. In DLSM, each spring bond is made up of one normal spring and one shear spring. The spring stiffness matrix at the local coordinate is written as:

$$\mathbf{K}_{\text{bond}} = \begin{pmatrix} k_n & 0 \\ 0 & k_s \end{pmatrix} \tag{19}$$

where k_n is the normal stiffness and k_s is the shear stiffness. The relationship between the spring parameters and the macro elastic constants, or Young's modulus and Poisson's ratio, is given as:

DOI: 10.1002/nag

$$k_n = \frac{2E}{\alpha^{2D}(1-\nu)} \tag{20}$$

and:

$$k_s = \frac{2(1-3\nu)E}{\alpha^{2D}(1-\nu^2)} \tag{21}$$

for plane-stress problems and:

$$k_n = \frac{2E}{\alpha^{2D}(1+\nu)(1-2\nu)} \tag{22}$$

and:

$$k_s = \frac{2(1-4\nu)E}{\alpha^{2D}(1+\nu)(1-2\nu)} \tag{23}$$

for plane-strain problems, where E is the Young's modulus, v is the Poisson's ratio, and α^{2D} is a lattice coefficient. Given the geometric data of the lattice spring model, α^{2D} is calculated as:

$$\alpha^{2D} = \frac{\sum_{i=1}^{N_b} l_i^2}{A} \tag{24}$$

where l_i is the original length of the ith bond, N_b is the number of spring bonds, and A is the total area of the lattice model. Equations (20) to (24) were derived based on the energy equivalence principle. Further details on the derivation can be found in the Appendix B of [27].

The strain energy stored in the spring bond is:

$$\Pi_b = \frac{1}{2}\widehat{\mathbf{u}}^{\,T}\mathbf{K}_{\text{bond}}\,\widehat{\mathbf{u}} = \frac{1}{2}(\mathbf{C}(\mathbf{u})\mathbf{u})^T\mathbf{K}_{\text{bond}}\mathbf{C}(\mathbf{u})\mathbf{u} \tag{25}$$

The total energy in the bond can then be written as:

$$\Pi = \Pi_b + \Pi_f = \frac{1}{2}(\mathbf{C}(\mathbf{u})\mathbf{u})^{\mathrm{T}}\mathbf{K}_{\text{bond}}\mathbf{C}(\mathbf{u})\mathbf{u} - \mathbf{f}(\mathbf{u})^{\mathrm{T}}\mathbf{u} \tag{26}$$

where Π_f is the virtual work done by the external force and $\mathbf{f}(\mathbf{u})$ is the external force vector of the particles.

According to the energy minimisation principle, we have:

$$\frac{\Pi}{\partial u_i} = \left(\mathbf{C}(\mathbf{u})\frac{\mathbf{u}}{\partial u_i} + \frac{\mathbf{C}(\mathbf{u})}{\partial u_i}\mathbf{u}\right)^{\mathrm{T}}\mathbf{K}_{\text{bond}}\mathbf{C}(\mathbf{u})\mathbf{u} - \left(\mathbf{f}(\mathbf{u})^{\mathrm{T}}\frac{\mathbf{u}}{\partial u_i} + \frac{\mathbf{f}(\mathbf{u})^{\mathrm{T}}}{\partial u_i}\mathbf{u}\right) = 0 \tag{27}$$

Let the general stiffness matrix be:

$$\hat{\mathbf{K}} = \left(\mathbf{C}(\mathbf{u})\frac{\mathbf{u}}{\partial u_i} + \frac{\mathbf{C}(\mathbf{u})}{\partial u_i}\mathbf{u}\right)^{\mathrm{T}}\mathbf{K}_{\text{bond}}\mathbf{C}(\mathbf{u}) \tag{28}$$

and the general force term be:

$$\hat{\mathbf{f}} = \mathbf{f}(\mathbf{u})^{\mathrm{T}}\frac{\mathbf{u}}{\partial u_i} + \frac{\mathbf{f}(\mathbf{u})^{\mathrm{T}}}{\partial u_i}\mathbf{u} = \mathbf{f}(\mathbf{u}) + \frac{\mathbf{f}(\mathbf{u})}{\partial u_i}\mathbf{u} \tag{29}$$

DOI: 10.1002/nag

Then, Equation (27) can be written as:

$$\hat{\mathbf{K}}\mathbf{u} = \hat{\mathbf{f}} \tag{30}$$

which is the classical form of the system equations in a numerical method. Figure 3 illustrates the physical meaning of Equation (30), where the **x** axis represents the position vector of the geometric model and **u** is the deformation vector. It can be seen that $\hat{\mathbf{K}}$ is the secant stiffness matrix. As shown in Figure 3, when $\mathbf{u} \to 0$, $\hat{\mathbf{K}}$ is equal to the tangent stiffness matrix. We now prove that $\hat{\mathbf{K}}\big|_{\mathbf{u}\to 0}$ is the same in the DLSM's stiffness matrix under a small deformation.

First, $\mathbf{u} \to 0$ indicates that the deformation and rigid rotation ω are small. Applying the first-order Tarler expansion of ω over $\cos(\omega)$ and $\sin(\omega)$ gives:

$$\cos(\omega) = \cos(0+\omega) \approx \cos(0) + (-\sin(0))\omega = 1 \tag{31}$$

$$\sin(\omega) = \sin(0+\omega) \approx \sin(0) + (\cos(0))\omega = \omega \tag{32}$$

Substituting Equations (31) and (32) into Equation (9), we have:

$$\begin{aligned}
\begin{pmatrix} u^{AB} \\ v^{AB} \end{pmatrix} &= \underbrace{\begin{pmatrix} 0 & -\omega \\ \omega & 0 \end{pmatrix}\begin{pmatrix} x^A - x^B \\ y^A - y^B \end{pmatrix}}_{\text{rigid rotation term}} + \underbrace{\begin{pmatrix} 1 & \omega \\ -\omega & 1 \end{pmatrix}\left(\begin{pmatrix} x^A - x^B & 0 \\ 0 & y^A - y^B \end{pmatrix}\begin{pmatrix} \hat{\varepsilon}_x \\ \hat{\varepsilon}_y \end{pmatrix} + \begin{pmatrix} y^A - y^B \\ x^A - x^B \end{pmatrix}\hat{\varepsilon}_{xy}\right)}_{\text{deformation term}} \\
&= \underbrace{\omega\begin{pmatrix} 0 & -1 \\ 1 & 0 \end{pmatrix}\begin{pmatrix} x^A - x^B \\ y^A - y^B \end{pmatrix}}_{\text{rigid rotation term}} + \underbrace{\begin{Bmatrix} 1 & 0 \\ 0 & 1 \end{Bmatrix}\left(\begin{pmatrix} x^A - x^B & 0 \\ 0 & y^A - y^B \end{pmatrix}\begin{pmatrix} \hat{\varepsilon}_x \\ \hat{\varepsilon}_y \end{pmatrix} + \begin{pmatrix} y^A - y^B \\ x^A - x^B \end{pmatrix}\hat{\varepsilon}_{xy}\right)}_{\text{deformation term}} \\
&\quad + \underbrace{\omega\begin{Bmatrix} 0 & 1 \\ -1 & 0 \end{Bmatrix}\left(\begin{pmatrix} x^A - x^B & 0 \\ 0 & y^A - y^B \end{pmatrix}\begin{pmatrix} \hat{\varepsilon}_x \\ \hat{\varepsilon}_y \end{pmatrix} + \begin{pmatrix} y^A - y^B \\ x^A - x^B \end{pmatrix}\hat{\varepsilon}_{xy}\right)}_{\text{deformation term } (O^2)}
\end{aligned} \tag{33}$$

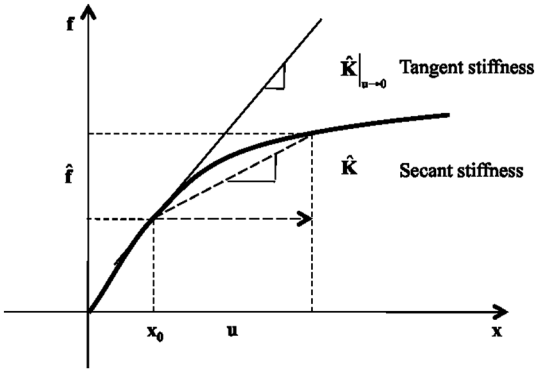

Figure 3. Secant and tangent stiffness of the DLSM under a large deformation.

DOI: 10.1002/nag

For small deformations, the final term is an O^2 term and Equation (33) can be further written as:

$$\begin{pmatrix} u^{AB} \\ v^{AB} \end{pmatrix} = \underbrace{\begin{pmatrix} 1 & 0 \\ 0 & 1 \end{pmatrix}\left(\begin{pmatrix} x^A - x^B & 0 \\ 0 & y^A - y^B \end{pmatrix}\begin{pmatrix} \hat{\varepsilon}_x \\ \hat{\varepsilon}_y \end{pmatrix} + \begin{pmatrix} y^A - y^B \\ x^A - x^B \end{pmatrix}\hat{\varepsilon}_{xy}\right)}_{\text{deformation term}} + \underbrace{\omega\begin{pmatrix} 0 & -1 \\ 1 & 0 \end{pmatrix}\begin{pmatrix} x^A - x^B \\ y^A - y^B \end{pmatrix}}_{\text{rigid rotation term}}$$
$$= \underbrace{\begin{pmatrix} x^A - x^B & 0 \\ 0 & y^A - y^B \end{pmatrix}\begin{pmatrix} \hat{\varepsilon}_x \\ \hat{\varepsilon}_y \end{pmatrix} + \begin{pmatrix} y^A - y^B \\ x^A - x^B \end{pmatrix}\hat{\varepsilon}_{xy}}_{\text{deformation term}} + \underbrace{\begin{pmatrix} -(y^A - y^B) \\ x^A - x^B \end{pmatrix}\omega}_{\text{rigid rotation term}} \tag{34}$$

When $\mathbf{u} \to 0$, the rigid rotation is close to zero, so the objective Cauchy strain $(\hat{\varepsilon}_x, \hat{\varepsilon}_y, \hat{\varepsilon}_{xy}) \to (\varepsilon_x, \varepsilon_y, \varepsilon_{xy})$. Equation (34) can then be written as:

$$\begin{pmatrix} u^{AB} \\ v^{AB} \end{pmatrix} = \underbrace{\begin{pmatrix} x^A - x^B & 0 \\ 0 & y^A - y^B \end{pmatrix}\begin{pmatrix} \varepsilon_x \\ \varepsilon_y \end{pmatrix} + \begin{pmatrix} y^A - y^B \\ x^A - x^B \end{pmatrix}\varepsilon_{xy}}_{\text{deformation term}} + \underbrace{\begin{pmatrix} -(y^A - y^B) \\ x^A - x^B \end{pmatrix}\omega}_{\text{rigid rotation term}} \tag{35}$$

By removing the rigid rotation term, the spring bond deformation can be written as:

$$\begin{Bmatrix} \overline{u}^{AB} \\ \overline{v}^{AB} \end{Bmatrix} = \begin{Bmatrix} x^A - x^B & 0 \\ 0 & y^A - y^B \end{Bmatrix}\begin{Bmatrix} \varepsilon_x \\ \varepsilon_y \end{Bmatrix} + \begin{Bmatrix} y^A - y^B \\ x^A - x^B \end{Bmatrix}\varepsilon_{xy} = \begin{Bmatrix} \varepsilon_x & \varepsilon_{xy} \\ \varepsilon_{xy} & \varepsilon_y \end{Bmatrix}\begin{Bmatrix} x^A - x^B \\ y^A - y^B \end{Bmatrix} \tag{36}$$

This equation can be further written in a vector form as:

$$\overline{\mathbf{u}} = [\boldsymbol{\varepsilon}]\cdot\mathbf{n}l \tag{37}$$

where $\mathbf{n}$ is the normal direction of the original spring bond and l is the length of the original spring bond.

The above equation is the DLSM formulation under small deformations [30]. Therefore, we have:

$$\mathbf{C}(\mathbf{u})|_{\mathbf{u}\to 0} = \mathbf{C} \tag{38}$$

The corresponding tangent stiffness matrix can then be written as:

$$[\mathbf{K}] = \left[\hat{\mathbf{K}}\right]\Big|_{\mathbf{u}\to 0} = \mathbf{C}^{\mathrm{T}}\mathbf{K}_{\mathrm{bond}}\mathbf{C} \tag{39}$$

which is the stiffness matrix of the DLSM under small deformations.

2.3. Internal spring bond force and unbalanced particle force

Assuming a general displacement field is given, the internal spring force of a bond can be calculated as:

$$\widehat{\mathbf{f}}^{\,\mathrm{inter}} = \begin{pmatrix} f^n \\ f^s \end{pmatrix} = \begin{pmatrix} k_n & 0 \\ 0 & k_s \end{pmatrix}\begin{pmatrix} u^n \\ u^s \end{pmatrix} \tag{40}$$

DOI: 10.1002/nag

This force can be further transformed into a model coordinate as:

$$\mathbf{f}^{\text{inter}} = \begin{pmatrix} f_x \\ f_y \end{pmatrix} = f^n \begin{pmatrix} n_x^3 \\ n_y^3 \end{pmatrix} + f^s \begin{pmatrix} -n_y^3 \\ n_x^3 \end{pmatrix} \tag{41}$$

The spring bond deformation can be calculated using Equations (11) to (13). However, this process involves complex computations and is targeted mainly at deriving the tangent stiffness matrix in section 2.2. A simplified formulation based on a vector operation is described here.

As shown in Figure 2, the vector of the original spring bond is $\overrightarrow{AB^0} = \left(x_B^0 - x_A^0, y_B^0 - y_A^0\right)$, while that of the current configuration is $\overrightarrow{AB^3} = \left(x_B^3 - x_A^3, y_B^3 - y_A^3\right)$ and the vector of the rigid rotated spring bond is $\overrightarrow{AB^2}^{\mathrm{T}} = \begin{pmatrix} \cos\omega & \sin\omega \\ -\sin\omega & \cos\omega \end{pmatrix} \overrightarrow{AB^0}^{\mathrm{T}} = \begin{pmatrix} \cos\omega & \sin\omega \\ -\sin\omega & \cos\omega \end{pmatrix} \begin{pmatrix} x_B^0 - x_A^0 \\ y_B^0 - y_A^0 \end{pmatrix}$. Then, the deformation of the spring bond can be written as:

$$\begin{pmatrix} u^{AB} \\ v^{AB} \end{pmatrix} = \overrightarrow{\Delta AB^3}^{\mathrm{T}} = \overrightarrow{AB^3}^{\mathrm{T}} - \overrightarrow{AB^2}^{\mathrm{T}} = \begin{pmatrix} x_B^3 - x_A^3 \\ y_B^3 - y_A^3 \end{pmatrix} - \begin{pmatrix} \cos\omega & \sin\omega \\ -\sin\omega & \cos\omega \end{pmatrix} \begin{pmatrix} x_B^0 - x_A^0 \\ y_B^0 - y_A^0 \end{pmatrix} \tag{42}$$

The spring bond deformation can now be obtained using Equation (42) together with Equations (11) and (20). The internal spring force is illustrated in Figure 4. Because both the normal and shear springs are used, the spring force is not central (see Figure 4). As shown in Figure 4, the unbalanced force on the particle is:

$$\mathbf{f}^{\text{un}} = \mathbf{f}^{\text{extern}} - \mathbf{f}^{\text{inter}} \tag{43}$$

Equation (43) applies only to a particle with a single spring bond. For a lattice network model, the total unbalanced force can be calculated as:

$$\mathbf{f}^{\text{un}} = \sum_{\Gamma} \mathbf{f}^{\text{extern}} - \sum_{N_b} \mathbf{f}^{\text{inter}} \tag{44}$$

where Γ represents the model boundary and *Nb* represents the model's spring bonds.

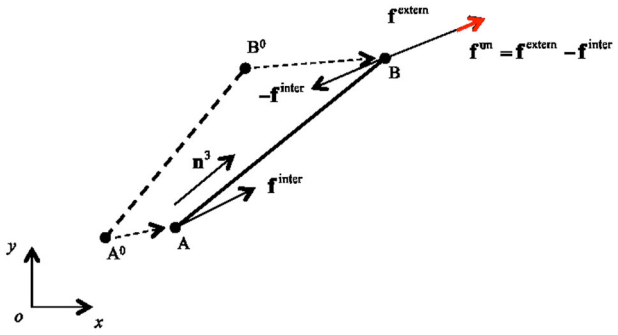

Figure 4. Internal force of a deformed bond and unbalanced force at a particle.

DOI: 10.1002/nag

2.4. Nonlinear solution methods

A large deformation DLSM is used to solve Equation (30), which is nonlinear. Many solution methods exist for a nonlinear equation, but this study adopts three classical methods: the Euler method, the modified Euler method, and the Newton method.

The Euler method is the simplest method of solving nonlinear problems. Figure 5 shows the basic principle of the Euler method. The first step is to divide the load into N steps. For each calculation step, the incremental displacement is calculated using the tangent stiffness matrix. The first step is calculated as:

$$\Delta \mathbf{u}_0 = \mathbf{K}(\mathbf{x}_0)^{-1}\mathbf{f}\left(\frac{1}{N}\bar{\mathbf{f}}, \mathbf{x}_0\right) \tag{45}$$

where $\bar{\mathbf{f}}$ is the loading vector, which is not changed by model deformations such as the application of pressure on the boundary.

The following steps (1 to $N-1$) are calculated as:

$$\Delta \mathbf{u}_i = \mathbf{K}\left(\mathbf{x}_0 + \sum_{j=0}^{i-1}\Delta \mathbf{u}_j\right)^{-1}\mathbf{f}\left(\frac{1}{N}\bar{\mathbf{f}}, \mathbf{x}_0 + \sum_{j=0}^{i-1}\Delta \mathbf{u}_j\right) \tag{46}$$

leading to a solution of:

$$\mathbf{u} = \sum_{i=0}^{N-1}\Delta \mathbf{u}_i \tag{47}$$

The Euler method is actually used to solve large deformations through a number of small deformation analyses. The RITSS method for FEM [6, 7] can be regarded as an example of the Euler method. The main advantages of this method are its robustness and simple implementation. However, it requires regular updating of the computational mesh and the corresponding stiffness matrix from conventional small strain analysis, and is a less precise method that may cause some errors in extremely large deformation analyses. These shortcomings will be discussed in the numerical example section of this paper. What follows is a discussion of an improved algorithm called the modified Euler method.

Figure 6 shows the basic principle of the modified Euler method. The first step is calculated as:

$$\Delta \bar{\mathbf{u}}_0 = \mathbf{K}(\mathbf{x}_0)^{-1}\mathbf{f}\left(\frac{1}{N}\bar{\mathbf{f}}, \mathbf{x}_0\right) \tag{48}$$

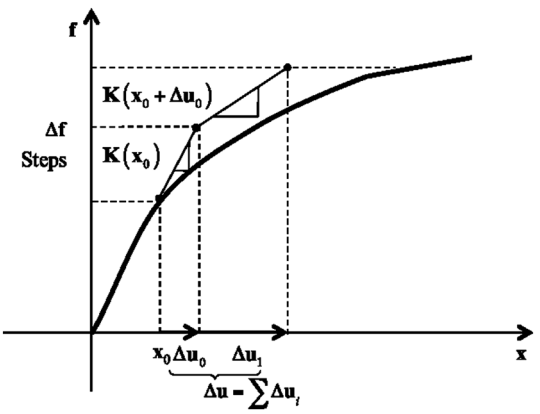

Figure 5. Euler method.

DOI: 10.1002/nag

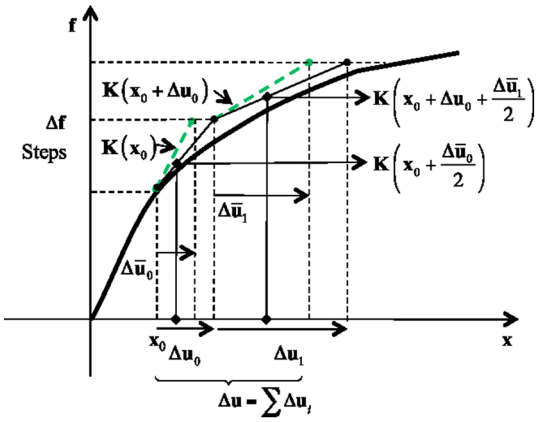

Figure 6. Modified Euler method.

$$\Delta \mathbf{u}_0 = \mathbf{K}\left(\mathbf{x}_0 + \frac{\Delta \bar{\mathbf{u}}_0}{2}\right)^{-1} \mathbf{f}\left(\frac{1}{N}\bar{\mathbf{f}}, \mathbf{x}_0 + \frac{\Delta \bar{\mathbf{u}}_0}{2}\right) \tag{49}$$

The following steps are calculated as:

$$\Delta \bar{\mathbf{u}}_i = \mathbf{K}\left(\mathbf{x}_0 + \sum_{j=0}^{i-1} \Delta \mathbf{u}_j\right)^{-1} \mathbf{f}\left(\frac{1}{N}\bar{\mathbf{f}}, \mathbf{x}_0 + \sum_{j=0}^{i-1} \Delta \mathbf{u}_j\right) \tag{50}$$

$$\Delta \mathbf{u}_i = \mathbf{K}\left(\mathbf{x}_0 + \sum_{j=0}^{i-1} \Delta \mathbf{u}_j + \frac{\Delta \bar{\mathbf{u}}_i}{2}\right)^{-1} \mathbf{f}\left(\frac{1}{N}\bar{\mathbf{f}}, \mathbf{x}_0 + \sum_{j=0}^{i-1} \Delta \mathbf{u}_j + \frac{\Delta \bar{\mathbf{u}}_i}{2}\right) \tag{51}$$

The modified Euler method requires the solving of two linear equations per calculation step. The solution can also be obtained from Equation (42).

The third solution method is called the Newton method or variation stiffness method. Figure 7 shows the principle of the Newton method. The first step calculation is:

$$\Delta \mathbf{u}_0 = \mathbf{K}(\mathbf{x}_0)^{-1} \mathbf{f}(\mathbf{x}_0) \tag{52}$$

For the *i*th step calculation, the unbalanced force is calculated as:

$$\mathbf{f}^{\text{un}}\left(\mathbf{x}_0 + \sum_{j=0}^{i-1} \Delta \mathbf{u}_j\right) = \mathbf{f}^{\text{ext}}\left(\mathbf{x}_0 + \sum_{j=0}^{i-1} \Delta \mathbf{u}_j\right) - \mathbf{f}^{\text{inter}}\left(\mathbf{x}_0 + \sum_{j=0}^{i-1} \Delta \mathbf{u}_j\right) \tag{53}$$

The displacement increment is:

$$\Delta \mathbf{u}_i = \alpha \mathbf{K}\left(\mathbf{x}_0 + \sum_{j=0}^{i-1} \Delta \mathbf{u}_j\right)^{-1} \mathbf{f}^{\text{un}}\left(\mathbf{x}_0 + \sum_{j=0}^{i-1} \Delta \mathbf{u}_j\right) \tag{54}$$

where α is a linear search coefficient that is used for convergence in the Newton method, the default value of which is 1.0 in this work.

DOI: 10.1002/nag

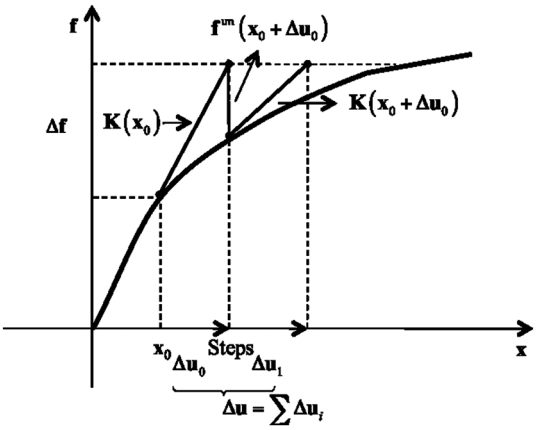

Figure 7. Newton method.

3. NUMERICAL EXAMPLES

In this section, examples of large deformation problems are solved using the developed lattice spring model. The results are compared with analytical solution and those obtained from the commercial FEM code ANSYS.

3.1. Beam bending under single point loading

The first example is a cantilever beam subject to a concentrated load problem. This is a classical benchmark problem used to test different numerical methods on large deformation analyses (e.g. [12–14]). Figure 8 shows the geometry and boundary conditions of this beam bending problem. The beam is of length $L = 10$ m and height $H = 1$ m. The left side of the beam is fixed in both the x- and y-directions. A concentrated load is applied at the top-left corner of the beam. The elastic constants of the beam, the Young's modulus and Poisson's ratio, are 1.0 GPa and 0.0, respectively, while the lattice size is 0.20 m. The analytical solution accounting for geometrical nonlinearity can be found in [33]. FEM solutions are obtained in ANSYS using triangular elements with a mesh size of 0.20 m. Figure 9 shows the results predicted by the analytical solution [32], the FEM (ANSYS) [34], and the large deformation DLSM using different solution methods. The results indicate that the DLSM, FEM, and analytical solutions are in good agreement and that the developed model is capable of solving large deformation problems. Figure 10 shows the deformed configurations of the DLSM under small and large deformation analyses. During the small deformation analysis (Figure 9a), the beam undergoes a relatively larger deflection in which the maximum y-direction displacement is 9.175 m. On the other hand, the maximum y-direction displacement of the large deformation DLSM is 7.098 m. Figure 9 shows that the large deformation analysis gives an accurate and reasonable displacement/deformation result, not results that are larger than that obtained from the small deformation analysis.

The analytical solution and a high-resolution FEM solution for the problem are used here as a reference for the convergence analysis of the developed large deformation DLSM, while an FEM model with a mesh size of 0.05 m is solved using FEM (ANSYS) in which the concentrated load is taken as 3000 kPa. The y-direction displacement along the bottom line of the beam is recorded and

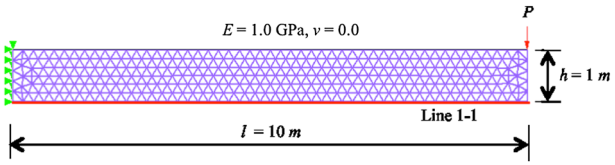

Figure 8. Geometry and boundary conditions of a cantilever beam subject to a concentrated load.

DOI: 10.1002/nag

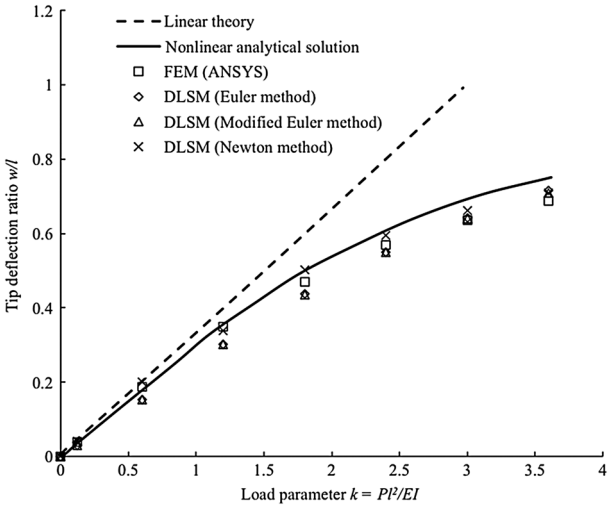

Figure 9. Large deflection analysis of a cantilever beam subjected to a concentrated load — results predicted by the analytical solution, FEM (ANSYS), and DLSM.

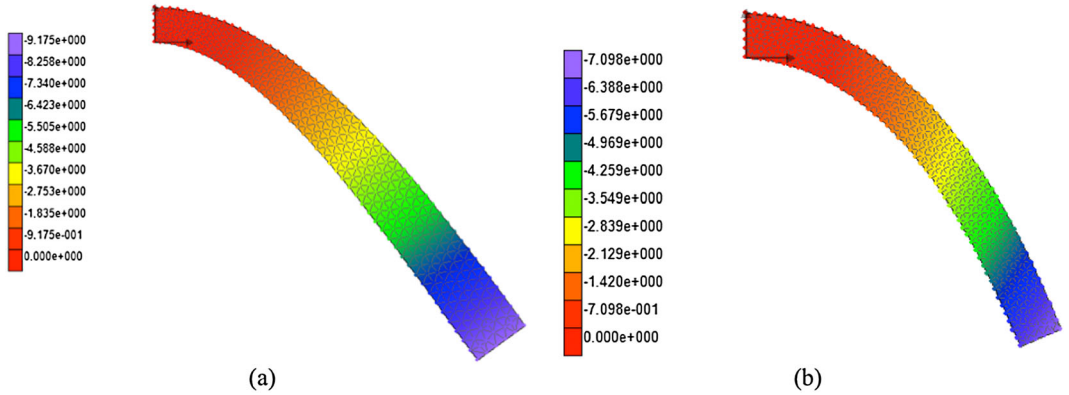

Figure 10. Deformed configurations (contour plot of y-direction displacement) predicted by DLSM: (a) small deformation analysis and (b) large deformation analysis.

three DLSM models with lattice sizes of 1.00 m, 0.50 m, and 0.20 m are used to solve the problem. The corresponding results of the DLSM and high-resolution FEM are plotted in Figure 11, which indicates that the DLSM solution quickly converges with the high-resolution FEM solution and the analytical solution with decreasing lattice size.

As shown in Figure 9, the different nonlinear solution methods produce slightly different solutions. To analyse the performance of these methods, the FEM (ANSYS) is used as the reference solution and the DSLM's percentage error is calculated as:

$$Err = \frac{\left|u^{DLSM} - u^{FEM}\right|}{\left|u^{FEM}\right|} \times 100\% \tag{55}$$

where u^{DLSM} is the top-left corner displacement calculated by DLSM and u^{FEM} is the value obtained using FEM (ANSYS). Table I lists the error of the DLSM calculated with different nonlinear solution methods for the beam bending problem, and indicates that the calculation error decreases as the load parameter increases for different nonlinear solution methods. The Euler method, modified Euler method, and Newton method produce very similar solutions when the load parameter is large, a difference that is apparent when the load parameter is small. These results show that the DLSM may be more suitable for large deformation analysis than small deformation analysis. The reason is

DOI: 10.1002/nag

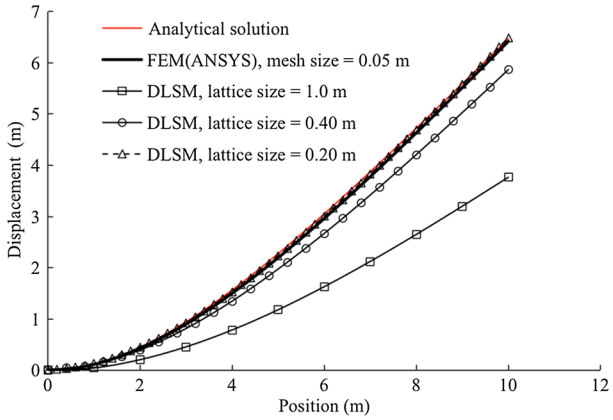

Figure 11. *y*-direction displacement along the bottom line of the beam predicted by the DLSM at different lattice sizes.

Table I. Numerical errors (%) of the DLSM when using different nonlinear solution methods compared with FEM (ANSYS) for the beam bending problem.

	Load parameter $k = Pl^2/EI$						
	0.12	0.60	1.20	1.80	2.40	3.00	3.60
Euler method	19.14	17.90	13.14	7.00	3.29	0.91	4.09
Modified Euler method	19.14	17.90	13.23	7.20	3.60	0.44	3.45
Newton method	7.25	7.37	3.08	7.01	4.43	3.78	3.43

that the DLSM has fully considered the influence of the rigid body rotation, which might become the dominant influence factor when the deformation is large (e.g. the beam bending problem).

To further examine the convergence of the different solution methods, the displacement of the beam's top-left tip under a concentrated load of 3000 kPa is compared to the total calculation steps. The results are listed in Table II and show that the results obtained from the different nonlinear solution methods achieve convergence as the total calculation steps increase. Here, the modified Euler method is the fastest at achieving convergence, requiring 20 steps. The Euler method is the worst and does not achieve convergence after 1000 steps (see Table II). The Newton method converges within 50 steps, placing its performance between that of the Euler and modified Euler methods. The displacement solutions obtained from the three methods are nearly identical in this example, with only a 0.06% difference between them that can be ignored for most applications. This result may be the reason why the Euler approach has been used to analyse large deformations in many practical applications like offshore foundations [6, 7]. However, because the Euler method does not check the final equilibrium condition during calculation, it may introduce large accumulated errors in extremely large deformation analyses. The following section presents a more challenging example to address this problem.

Table II. Vertical displacement at the beam's loading point obtained using DLSM with different nonlinear solution methods for the beam bending problem.

	Total calculation steps								
	2	5	10	20	30	40	50	100	1000
Euler method	0.9210	0.8011	0.7547	0.7320	0.7245	0.7208	0.7186	0.7143	**0.7103**
Modified Euler method	0.7355	0.7116	0.7101	**0.7099**	0.7099	0.7099	0.7099	0.7099	0.7099
Newton method	0.9325	0.6649	0.7884	0.7151	0.7102	0.7099	**0.7098**	0.7098	0.7098

DOI: 10.1002/nag

3.2. *Cantilever beam subjected to an end moment*

Figure 12 illustrates the problem of a cantilever beam to which a moment is applied at the end. The analytical solution is provided by Pai and Palazotto [35], who have reported that the initially straight cantilever is bent into a circular arc when the moment satisfies:

$$M = \frac{2\pi EI}{l} \tag{56}$$

where M is the applied moment, E is the beam's elastic modulus, I is the area moment of inertia, and l is the length of the beam. The lattice model used in this example is shown in Figure 12. The beam's length $l = 200$ m and height $h = 10$ m, and the lattice size is 0.25 m. The material properties include an elastic modulus $E = 5$ GPa and Poisson's ratio $v = 0.0$. The left side of the beam is fixed in both the x- and y-directions. Two opposite pressures are applied at the right side of the beam to produce a moment in it. From Equation (56), the applied pressure $p = 532.6$ MPa, which is calculated as:

$$p = \frac{2\pi Eh}{3l} \tag{57}$$

FEM (ANSYS) is used to solve the problem, but cannot achieve a converged solution. Figure 13 shows the final configuration for this beam moment bending problem obtained by ANSYS and shows that ANSYS cannot achieve a circular arc as expected, which may be due to the fact that the default nonlinear solver setting does not account for such extremely large deformation cases or the approximation of the rigid rotation in ANSYS [34, 36]. However, details on the reason for

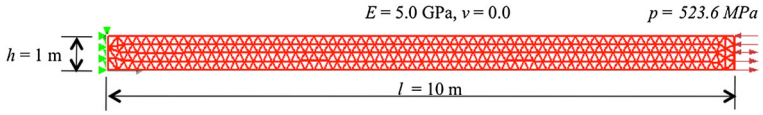

Figure 12. Geometry and boundary conditions of a cantilever beam subjected to an end moment.

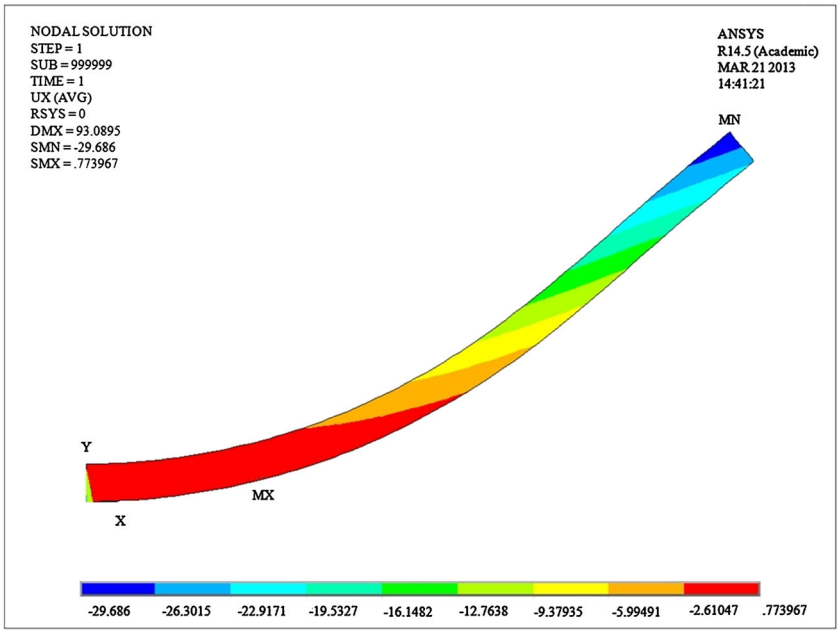

Figure 13. Deformed configuration of the beam moment bending problem predicted by FEM (ANSYS).

DOI: 10.1002/nag

ANSYS's failure are outside the scope of this paper. The large deformation DLSM is instead used to solve this problem, and the unbalanced force during calculation is reported here. An index is used to present the equilibrium condition of each calculation step and is called the ratio of unbalanced force:

$$R^{\mathrm{un}} = \frac{\max\left(\left|\mathbf{f}^{\mathrm{ext}} - \mathbf{f}^{\mathrm{inter}}\right|\right)}{\max\left(\left|\mathbf{f}^{\mathrm{ext}}\right|\right)} \tag{58}$$

where $\mathbf{f}^{\mathrm{ext}}$ is the external force at the calculation step and $\mathbf{f}^{\mathrm{inter}}$ is the internal force of the lattice network at the calculation step.

Figure 14 shows the results obtained using DLSM with the Euler method. The final configuration is closer to a circular arc than that in Figure 13. The ratio of unbalanced force during the calculation is shown in Figure 15, which shows that the ratio of unbalanced force is large for the Euler method, with a final value of 86.71%. Fortunately, the unbalanced force is not accumulated during the

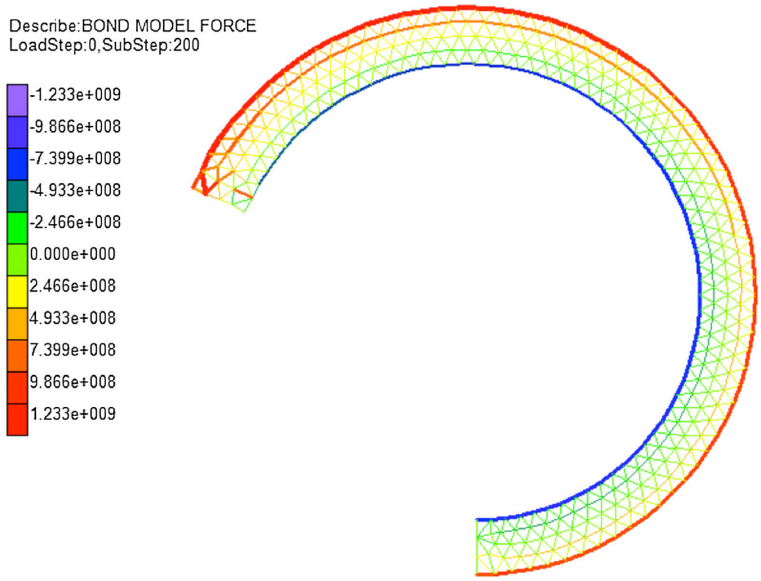

Figure 14. Deformed configuration of the beam moment bending problem obtained by DLSM with the Euler method.

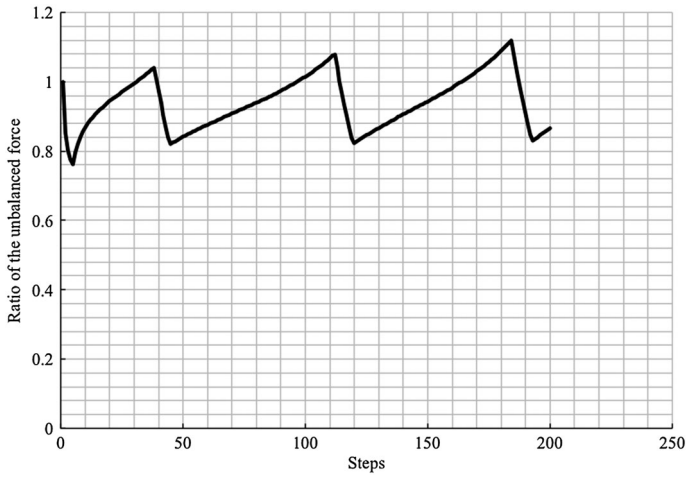

Figure 15. Curve of the ratio of unbalanced force for the beam moment bending problem predicted by the DLSM using the Euler method.

DOI: 10.1002/nag

calculation. Figures 16 and 17 show the results obtained with the modified Euler method and the history curve for the ratio of unbalanced force during calculation, and show that the modified Euler method generates a very similar configuration to that of the Euler method. However, the final ratio of unbalanced force for the modified Euler method is 40.45%. Figures 18 and 19 show the results obtained using the Newton method. The final deformed shape is close to a circle and the final ratio of unbalanced force is 0.14% ($\alpha = 0.1$). This example indicates the importance of minimising the unbalances force in this problem.

3.3. Rectangle framework subjected to compression

In the previous examples, in order to compare with analytical solutions, the Poisson's ratios are taken to be zero. In this section, a more complex example is presented. Figure 20 shows the geometry, the loading condition, and the lattice model for the problem. The elastic constants are elastic modulus $E = 25$GPa and Poisson's ratio $v = 0.2$. Results of FEM (ANSYS), DLSM (small deformation), and

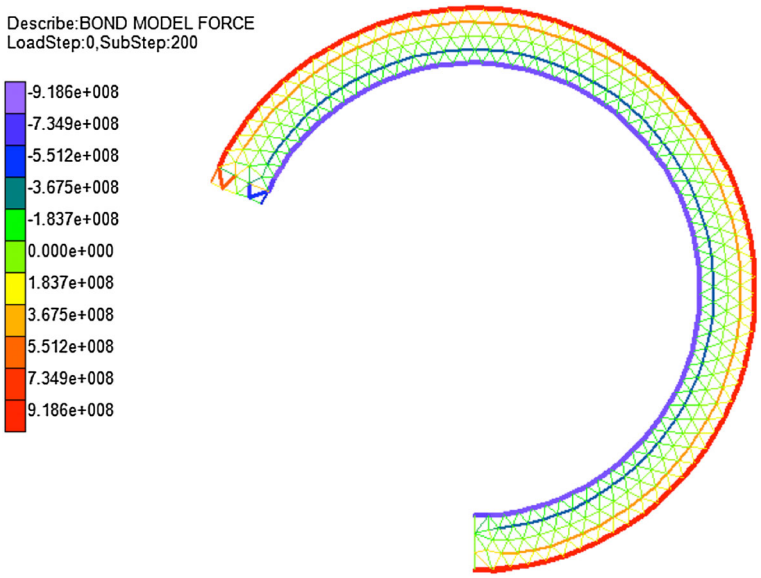

Figure 16. Deformed configuration of the beam moment bending problem obtained by DLSM with the modified Euler method.

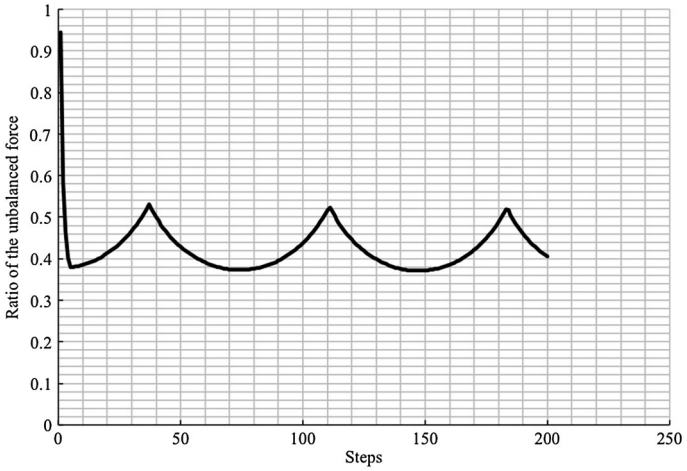

Figure 17. Curve of the ratio of unbalanced force for the beam moment bending problem predicted by the DLSM using the modified Euler method.

DOI: 10.1002/nag

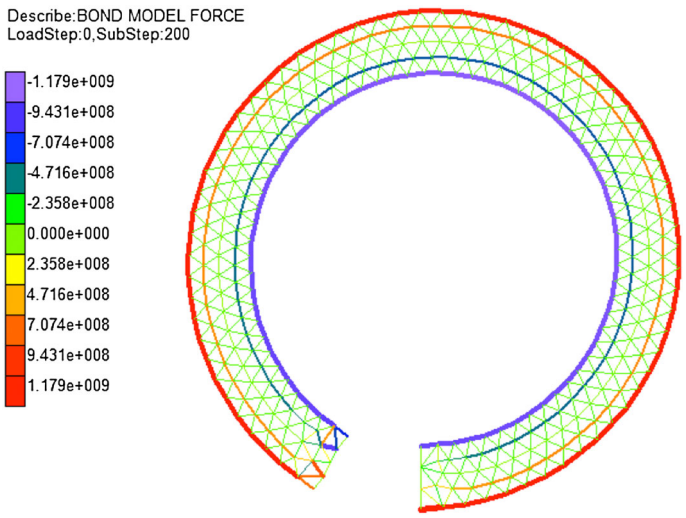

Figure 18. Deformed configuration of the beam moment bending problem obtained by DLSM with the Newton method.

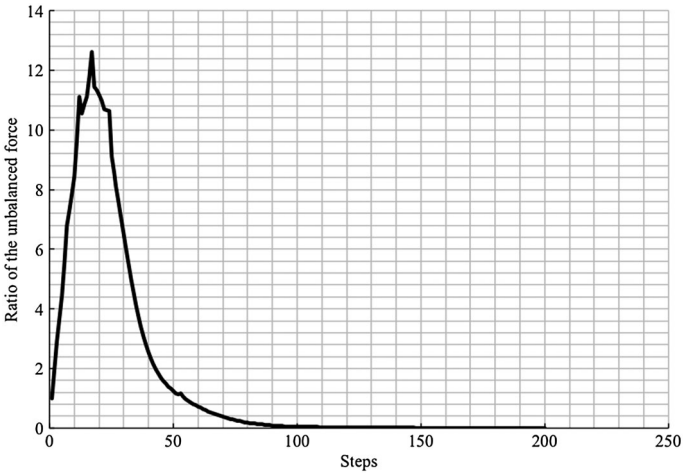

Figure 19. Curve of the ratio of unbalanced force for the beam moment bending problem predicted by the DLSM using the Newton method.

the DLSM for large deformation are presented in Figure 21. Again, good match between the results by FEM (ANSYS) and the DLSM for large deformation. The coupled modified Euler and Newton method is adopted in this example. The problem would first be calculated using the modified Euler method and then by the Newton method to minimise the unbalanced force. A total of 20 cycles (10 for modified Euler and 10 for Newton method, $\alpha = 1.0$) are used to get the convergence. The results of small deformation DLSM are much less than the results predicted by FEM (ANSYS) (see Figure 25). This problem is similar to the concrete/steel support design for underground structures. The serviceability of support structure is mainly controlled by the maximum deformation. From this example, it shows that the small deformation analysis produces a very smaller value; thus, it may provide an unsafe design. Moreover, force chain of the problem predicted by the DLSMs for small and large deformation analysis is presented in Figure 22, respectively. The maximum compressive and tensile force for the large deformation DLSM is much higher than these by the small deformation DLSM. Therefore, for the strength/safety design, the small deformation analysis may also lead in an over optimistic design. This example reaffirmed the importance of large deformation analysis.

DOI: 10.1002/nag

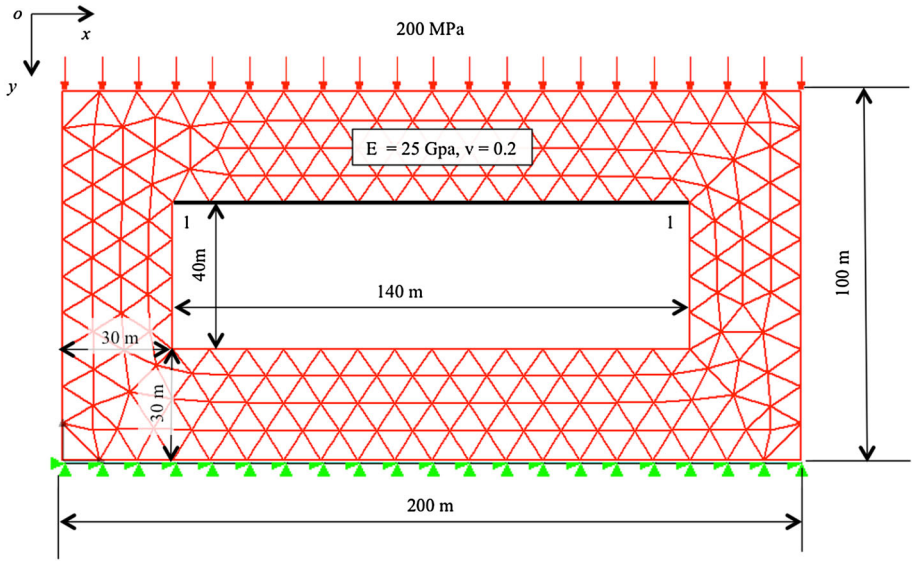

Figure 20. Geometry and boundary conditions for a rectangle framework under compression.

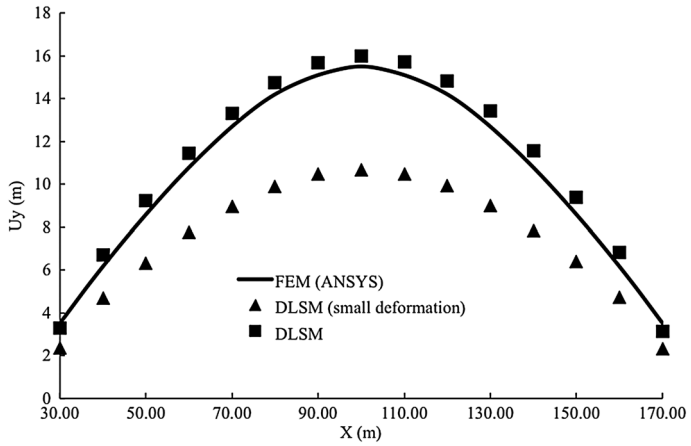

Figure 21. The *y*-direction displacement along the line 1–1 of the rectangle framework predicted by FEM (ANSYS), the DLSM for small deformation [30], and DLSM with coupled modified Euler and Newton method for large deformation analysis.

Besides the LSM has advantage on fracturing simulations of solid, compared with the classical FE method, they are also very straightforward for implementation and understanding. For instance, the FE method usually adopted the second Piola–Kirchoff stress tensor in large deformation analysis while the LSM can still use the same definition of spring force. There are also some practical problems that have to consider both the fracturing and large deformation, e.g. the failure of rock strata and underground structure in deep mining. However, the LSM is also not perfect. One of the main shortcomings is the insufficient development of advanced constitutive model. Nonlinear springs can be used in LSM to describe the nonlinear behaviour of materials. However, it was found that the ratio of compressive strength to tensile strength predicted by LSM with nonlinear spring is still much lower than that of rock materials (typically around 10–12) [37]. Therefore, to further develop local complex bond constitutive model for LSM is essential to realistically model the nonlinear behaviour of materials such as soil and rock.

DOI: 10.1002/nag

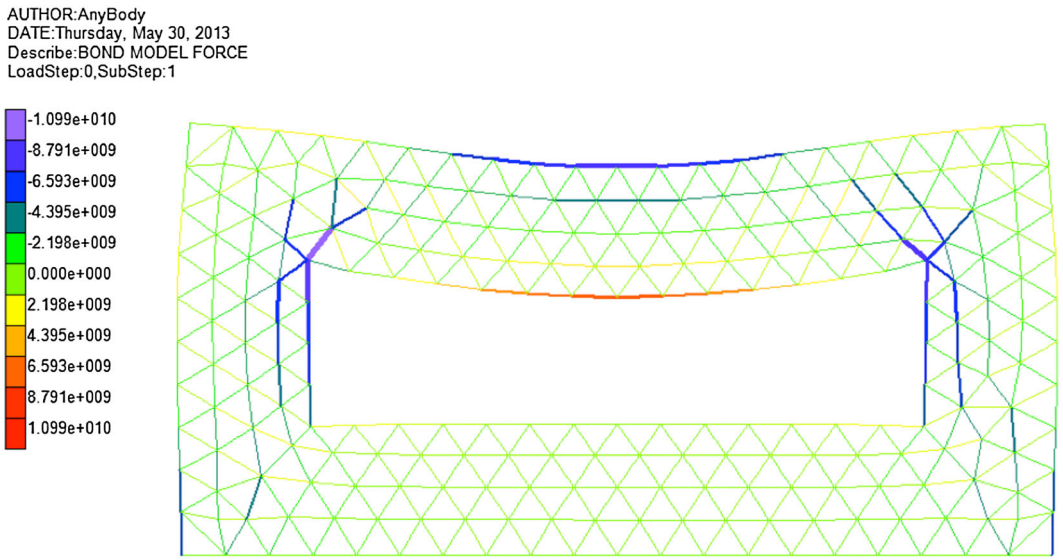

(a)

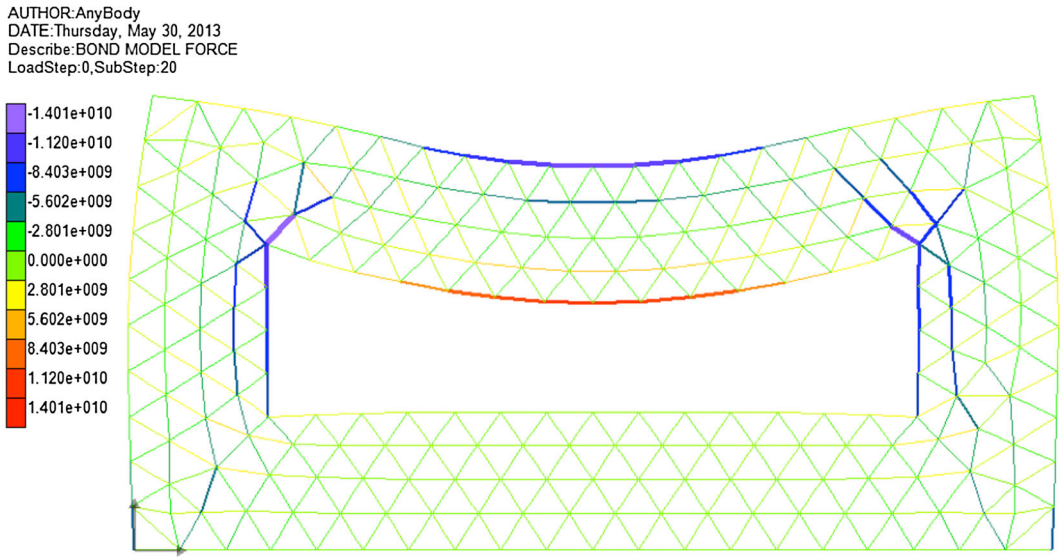

(b)

Figure 22. Force chain for the rectangle framework problem predicted by the DLSM for small deformation [30] and the DLSM for large deformation analysis: (a) the DLSM for small deformation [30] and (b) the DLSM with coupled modified Euler and Newton method.

4. CONCLUSIONS

This paper presents a large deformation LSM, the spring bond deformation of which under large deformations is derived using polar decomposition. Next, the stiffness matrix under large deformations is derived. The tangent stiffness matrix is further proven to be equal to the stiffness matrix under small deformations. Three different nonlinear solution methods are proposed based on these processes and two well-known benchmark problems are calculated using the proposed model. The results show that the model is capable of solving large deformation problems. The performances of different nonlinear solution methods are also investigated. The Euler method is simple to implement but computationally inefficient. The Newton method is the most precise, while

DOI: 10.1002/nag

the modified Euler method is the most robust. A combination of the modified Euler and Newton methods can result in better performance.

ACKNOWLEDGEMENTS

This research is financially supported by the Australian Research Council (Grant No. DE130100457) and the State Key Laboratory of Coal Resources and Safe Mining, CUMT (Grant No. SKLCRSM11KFA02).

REFERENCES

1. Hibbitt HD, Marcal PV, Rice JR. A finite element formulation for problems of large strain and large displacement. *International Journal of Solids and Structures* 1970; **6**:1069–1086.
2. Bathe KJ, Ramm E, Wilson EL. Finite element formulations for large deformation dynamic analysis. *International Journal for Numerical Methods in Engineering* 1975; **9**:353–286.
3. McMeeking RM, Rice JR. Finite-element formulations for problems of large elastic–plastic deformation. *International Journal of Solids and Structures* 1975; **11**:601–616.
4. Kojic M, Bathe KJ. Studies of finite element procedures--Stress solution of a closed elastic strain path with stretching and shearing using updated Lagrangian Jaumann formulation. *Computers and Structures* 1987; **26**:175–179.
5. Gadala MS, Wang J. ALE formulation and its application in solid mechanics. *Computer Methods in Applied Mechanics and Engineering* 1998; **167**:33–55.
6. Hu Y, Randolph MF. A practical numerical approach for large deformation problems in soil. *International Journal for Numerical and Analytical Methods in Geomechanics* 1998; **22**:327–350.
7. Nazem M, Carter JP, Sheng D, Sloan SW. Alternative stress-integration schemes for large-deformation problems of solid mechanics. *Finite Elements in Analysis and Design* 2009; **45**:934–943.
8. Alsafadie R, Hjiaj M, Battini JM. Corotational mixed finite element formulation for thin-walled beams with generic cross-section. *Computer Methods in Applied Mechanics and Engineering* 2010; **199**:3197–3212.
9. Novati G, Brebbia CA. Boundary element formulation for geometrically nonlinear elastostatics. *Applied Mathematical Modelling* 1982; **6**:136–138.
10. Chandra A, Mukhejee S. Boundary element formulation for large strain-large deformation of viscoplasticity. *International Journal of Solids and Structures* 1984; **30**:41–53.
11. Xie HP. Analysis of nonlinear large deformation problems by boundary element method. *Applied Mathematics and Mechanics* 1988; **9**:1153–1161.
12. Liew KM, Ng TY, Wu YC. Meshfree method for large deformation analysis- a reproducing kernel particle approach. *Engineering Structures* 2002; **24**:543–551.
13. Gu YT. An adaptive local meshfree updated Lagrangian approach for large deformation analysis of metal forming. *Advanced Materials Research* 2010; **97–101**:2664–2667.
14. Khoshghalb A. Meshfree analysis of unsaturated porous media including hydraulic hysteresis and large deformations, PhD thesis, 2011, UNSW, Australia, Sydney.
15. Moresi L, Dufour F, Muhlhaus HB. A Lagrangian integration point finite element method for large deformation modeling of viscoelastic geomaterials. *Journal of Computational Physics* 2003; **184**:476–497.
16. Cho JR, Lee HW. 2-D large deformation analysis of nearly incompressible body by natural element method. *Computers and Structures* 2006; **84**:293–304.
17. Gu YT, Wang QX, Lam KY. A meshless local Kriging method for large deformation analyses. *Computer Methods in Applied Mechanics and Engineering* 2007; **196**:1673–1684.
18. Luo YH. Dealing with extremely large deformation by Nearest-Nodes FEM with algorithm for updating element connectivity. *International Journal of Solids and Structures* 2008; **45**:5074–5087.
19. Liu YN, Sun L, Xu F, Liu YH, Cen ZZ. B spline-based method for 2-D Large deformation analysis. *Engineering Analysis with Boundary Elements* 2011; **35**:761–767.
20. Haber RB. A mixed Eulerian–Lagrangian displacement model for large deformation analysis in solid mechanics. *Computer Methods in Applied Mechanics and Engineering* 1984; **43**:277–292.
21. Hrennikoff A. Solution of problems of elasticity by the framework method. *ASME Journal of Applied Mechanics* 1941; **8**:A619–A715.
22. Zhao GF. Development of micro–macro continuum-discontinuum coupled numerical method. PhD Thesis. 2010, EPFL, Switzerland.
23. Zhao SF, Zhao GF. Implementation of a high order lattice spring model for elasticity. *International Journal of Solids and Structures* 2012; **49**:2568–2581.
24. Selle A, Su J, Irving G, Fedkiw R. Robust high-resolution cloth using parallelism, history-based collisions, and accurate friction. *IEEE TVCG.* 2009; **15**:339–350.
25. Selle A, Lentine MG, Fedkiw R. A mass spring model for hair simulation. ACM Trans. Graphics SIGGRAPH. *ACM TOG* 2008; **27**:64.1–64.11.
26. Holecek M, Moravec F. Hyperelastic model of a material which microstructure is formed by "balls and springs". *International Journal of Solids and Structures* 2006; **43**:7393–7406.
27. Hou P. Lattice model applied to the fracture of large strain composite. *Theoretical and Applied Fracture Mechanics* 2007; **47**:233–243.

DOI: 10.1002/nag

28. Patete P, Iacono MI, Spadea MF, Trecate G, Vergnaghi D, Mainardi LT, Baroni G. A multi-tissue mass-spring model for computer assisted breast surgery. *Medical Engineering and Physics* 2012. doi:10.1016/j.medengphy.2012.03.008.
29. Zhao GF, Fang J, Zhao J. A 3D distinct lattice spring model for elasticity and dynamic failure. *International Journal for Numerical and Analytical Methods in Geomechanics* 2011; **35**:859–885.
30. Zhao GF, Fang J, Zhao J. A MLS-based lattice spring model for simulating elasticity of materials. *International Journal for Computational Methods* 2012; **09**:1250037_01-1250037_22. doi:10.1142/S0219876212500375.
31. Zhao GF, Khalili N. A lattice spring model for coupled fluid flow and deformation problems in geomechanics. *Rock Mechanics and Rock Engineering* 2012; **45**:781–709.
32. Perngjin FP, Anthony NP, James MGJ. Polar decomposition and appropriate strains and stresses for nonlinear structural analyses. *Computers and Structures* 1998; **66**:823–840.
33. Bathe KJ, Bolourch S. Large displacement analysis of three-dimensional beam structures. *International Journal for Numerical Methods in Engineering* 1979; **14**:961–986.
34. ANSYS Inc. Theory reference-Large deformation analysis, ANSYS User's Manual, 2012.
35. Pai PF, Palazotto AN. Large deformation analysis of flexible beams. *International Journal of Solids and Structures* 1996; **33**:1335–1353.
36. Hughes TJR, Winget J. Finite rotation effects in numerical integration of rate constitutive equations arising in large-deformation analysis. *International Journal for Numerical Methods in Engineering* 1980; **15**:1862–1867.
37. Zhao GF, Fang J, Sun L, Zhao J. Parallelization of the distinct lattice spring model. *International Journal for Numerical and Analytical Methods in Geomechanics* 2013; **37**:51–74.

DOI: 10.1002/nag